Received: 17 May 2023 | Revised: 19 September 2023 | Accepted: 21 October 2023

DOI: 10.1002/mrm.29921

RESEARCH ARTICLE

Magnetic Resonance in Medicine

Minimization of eddy power loss in the cryostat for a z-gradient array coil driven by an arbitrary pulse sequence: An electromagnetic approach

Manouchehr Takrimi[1] | **Ergin Atalar**[1,2]

[1]National Magnetic Resonance Research Center (UMRAM), Bilkent University, Ankara, Turkey

[2]Department of Electrical and Electronics Engineering, Bilkent University, Ankara, Turkey

Correspondence
Manouchehr Takrimi, National Magnetic Resonance Research Center (UMRAM), Bilkent University, 06800 Bilkent, Ankara, Turkey.
Email: mtakrimi@bilkent.edu.tr

Funding information
Türkiye Bilimsel ve Teknolojik Araştırma Kurumu, Grant/Award Number: 121E128

Abstract

Purpose: This paper presents a novel computational approach to optimize gradient array performance for a given pulse sequence. Specifically, we propose an electromagnetic (EM) approach that minimizes eddy losses within the cryostat while maintaining key performance parameters such as field linearity, gradient strength, and imaging region's dimension and position.

Methods: High-resolution EM simulations on the cryostat's surface are deployed to compute the net EM fields generated by each element of a gradient array coil at different frequencies. The computed fields are stored and combined for each frequency to form a quadratic vector–matrix–vector computation. The overall time-average eddy power loss within the cryostat assembly for arbitrary pulse sequences is computed using frequency domain superposition.

Results: The proposed approach estimates and regulates eddy power losses within the cryostat assembly. When compared to the stray field minimization approach, it can achieve over twice the reduction in eddy power loss. The proposed approach eliminates the need to sample the stray fields on the cryostat surface, which the number and position of the samples would be challenging when designing tunable array coils with capabilities that disrupt field symmetries. Additionally, the loss calculation considers the entire cryostat assembly rather than just the inner cylindrical surface of the warm shield.

Conclusion: Our findings highlight the efficacy of an on-the-fly tuning method for the development of high-performance whole-body gradient array coils, effectively mitigating eddy losses within the cryostat and minimizing stray fields outside the coil assembly. This approach proves particularly advantageous for array coils with variable feeding currents.

KEYWORDS

eddy loss, gradient field optimization, MRI gradient array coil, Poynting theorem

1 | INTRODUCTION

Modern high-performance whole-body gradient coils are designed with active-shield coils to screen the fields generated by the primary coils such that the forces and torques are balanced and the desired gradient fields are confined inside the region of interest (ROI) with a minimum stored magnetic energy and copper losses as well as minimum stray fields outside the coil assembly. Meanwhile, the warm shield of the cryostat not only provides a solid cylindrical bed for the gradient coil but also serves as an additional passive screening wall, safeguarding the inner cold shield of the superconducting magnet from eddy currents induced by fast-switching stray fields generated by multiple layers of gradient coils. Different analytic or numerical methodologies[1] have been published to address the calculation and design of active-shield gradient coils where the wire (strip) profiles are adjusted to minimize the stray fields around the cryostat and optimize some performance parameters like gradient intensity, field linearity, and ROI size. Many of these approaches are based on the well-known target-field method.[2,3] Analytic eddy current calculations combined with the stream-function method were also formulated.[4]

The above design strategies work well for conventional coils with a fixed magnetic field profile. However, in array coils[5–10] the feeding currents of the primary and shield array elements are variable and depend on the required magnetic profile at the time of imaging.[7–11] Such on-the-fly profile tuning poses the challenge of minimizing stray magnetic fields near the warm shield while maintaining the required performance parameters. The main challenge is determining the number of target field points required to achieve satisfactory performance parameters within the ROI while minimizing stray fields on (and around) the warm shield's surface.[12] Another design challenge is the sensitivity of the solution to the number and location of stray field sampling points around the cryostat. Note that the total field sampling points can be significantly reduced (by a factor of eight for both x- and y-gradient coils) without compromising optimization, thanks to the inherent even/odd symmetries of conventional gradient coils. To further reduce the calculations for the z-gradient coil, 2D models (rather than 3D) can be used. Unfortunately, when array coils' new capabilities enter the picture, most of these reductions become inapplicable because the array gradient coils[11] are designed and optimized to address many new features that disrupt field symmetries (such as tuning the size, position, and linearity of the fields within the ROI). Furthermore, recent array-based gradient coils introduce new functionalities (such as regulating the peripheral nerve stimulation threshold[8] or reverse feeding of the shield coil to increase the slew rate) that redefine how we used them previously, necessitating the development of new and fast calculation methods to compensate for induced eddy currents.

In this work, using quadratic vector–matrix–vector multiplication, we propose a fast method to estimate and minimize the time-average eddy power losses within the warm shield of the cryostat assembly by optimizing the feeding currents. We demonstrate that based on the proposed approach, the number and location of stray field sampling points around the cryostat surface would no longer be an optimization target. Additionally, we show that the proposed approach is extendible for any pulse sequence using superposition in the frequency domain. In this work, the phasor notation with $e^{j\omega t}$ time convention is used and suppressed.

2 | METHODS

2.1 | Poynting theorem and eddy power loss calculation

We utilize the Poynting theorem[13] to calculate the time-average ohmic eddy power loss in the warm shield's metallic body. For a body composed of a nondispersive simple medium of volume V enclosed by surface(s) S, with no impressed sources inside, the time-harmonic integral form of the Poynting theorem reads:

$$\int_V \frac{1}{2}\left(\overline{E}\cdot\overline{J}^*\right)dv + j4\pi f\left[\int_V \frac{1}{4}\left(\overline{B}\cdot\overline{H}^*\right)dv - \int_V \frac{1}{4}\left(\overline{E}\cdot\overline{D}^*\right)dv\right] = -\oint_S \frac{1}{2}\left(\overline{E}\times\overline{H}^*\right)\cdot\hat{a}_n ds \quad (1)$$

where superscript $(\cdot)^*$ denotes complex conjugate, $\hat{a}_n$ is the outward normal unit vector on the closed surface S, $\overline{J}$ is the volume eddy current density, and f is the excitation frequency. The first term in the equation represents the time-average conversion of the electromagnetic energy generated by the gradient coils into thermal energy. The second and third terms account for the time-average stored (reactive) magnetic and electric energies within V. We assume that the permittivity ϵ, permeability μ, and conductivity σ are real constants (regardless of possible temperature dependency), and therefore, all three volume integrals are real. Four important aspects of using the Poynting theorem in the loss calculation are:

1. It only requires sampling the fields on the surface(s) of the specified volume rather than dealing with the spatial distribution of the fields within it.
2. Only the normal component of $\left(\overline{E}\times\overline{H}^*\right)$ with respect to the surface(s) is needed to carry out the integral.

3. $\mathrm{Re}\left\{-\oint_S \frac{1}{2}\left(\overline{E}\times\overline{H}^*\right)\cdot\hat{a}_n ds\right\}$ represents the time-average total ohmic power loss caused by induced eddy currents.
4. $\mathrm{Im}\left\{-\oint_S \frac{1}{2}\left(\overline{E}\times\overline{H}^*\right)\cdot\hat{a}_n ds\right\}$ returns the time-average stored magnetic energy within the volume (since the stored electric energy is negligible), which can be used as the secondary cost function to be optimized.

The net magnetic field, denoted as $\overline{H}$ in Eq. (1), encompasses different electromagnetic effects. These include nonuniform current distribution across wire cross-sections and the proximity effect when multi-turn wire bundles serve as array elements. This is where commercial full-wave electromagnetic (EM) solvers step in to handle these phenomena. The fields produced by each element of a gradient array coil in the presence of a cryostat are simulated and captured for a set of frequencies with an appropriate level of accuracy and spatial resolution. Once recorded, the collected data enables superposition, facilitating the computation of the net EM fields for all array elements under various excitations. This EM-based approach may require several hours of simulations, depending on the number of array elements and the mesh size, but it only has to be computed once.

2.2 | Eddy power loss calculation for a gradient array coil

Let $\bar{r}$ be the position vector specified by (ρ,φ,z) for an arbitrary point in cylindrical coordinates. If $\overline{E}(\bar{r}) = \left[E_\rho(\bar{r}), E_\varphi(\bar{r}), E_z(\bar{r})\right]$ and $\overline{H}(\bar{r}) = \left[H_\rho(\bar{r}), H_\varphi(\bar{r}), H_z(\bar{r})\right]$ represent the total net radial, circumferential, and axial time harmonic EM fields generated by all array elements at a given position $\bar{r}$ and frequency f, then the complex Poynting vector $\overline{\mathbb{P}} = \frac{1}{2}\overline{E}\times\overline{H}^*$ yields:

$$\overline{\mathbb{P}}(\bar{r},f) = \frac{1}{2}\left(E_\varphi H_z^* - E_z H_\varphi^*\right)\hat{a}_\rho + \frac{1}{2}\left(-E_\rho H_z^* + E_z H_\rho^*\right)\hat{a}_\varphi + \frac{1}{2}\left(E_\rho H_\varphi^* - E_\varphi H_\rho^*\right)\hat{a}_z. \tag{2}$$

The cylindrical symmetry of the cryostat assembly allows us to safely ignore the φ component in Eq. (2). The net EM field generated by the n^{th} array element is proportional to the excitation current A_n,where $n = 1..N$, and N is the total number of array elements. One can write an expression for the total net EM field generated by all array elements on the surface(s) of interest as:

$$F_u(\bar{r}) = \sum_{n=1}^{N} A_n F_{u_n}(\bar{r}) \tag{3}$$

where F stands for either of electric or magnetic field, the index u refers to any of its (ρ,φ,z) components, and F_{u_n} represent the net radial, circumferential, or axial EM field generated by the n^{th} array element with unit input excitation. Each of the four remaining Poynting terms in Eq. (2), namely, $E_\varphi H_z^*, E_z H_\varphi^*, E_\rho H_\varphi^*$, and $E_\varphi H_\rho^*$ is rewritten as a double summation using Eq. (3) as:

$$\overline{\mathbb{P}}(\overline{A},\bar{r},f) = \frac{1}{2}\left\{\sum_{n=1}^{N}\sum_{m=1}^{N} A_n\left[E_{\varphi_n}(\bar{r})H_{z_m}^*(\bar{r}) - E_{z_n}(\bar{r})H_{\varphi_m}^*(\bar{r})\right]A_m^*\right\}\hat{a}_\rho + \frac{1}{2}\left\{\sum_{n=1}^{N}\sum_{m=1}^{N} A_n\left[E_{\rho_n}(\bar{r})H_{\varphi_m}^*(\bar{r}) - E_{\varphi_n}(\bar{r})H_{\rho_m}^*(\bar{r})\right]A_m^*\right\}\hat{a}_z. \tag{4}$$

All four double summations in Eq. (4) are converted into quadratic form as:

$$\overline{\mathbb{P}}(\overline{A},\bar{r},f) = \frac{1}{2}\overline{A}\left(\overline{\overline{T}}_{\varphi z} - \overline{\overline{T}}_{z\varphi}\right)\overline{A}'\hat{a}_\rho + \frac{1}{2}\overline{A}\left(\overline{\overline{T}}_{\rho\varphi} - \overline{\overline{T}}_{\varphi\rho}\right)\overline{A}'\hat{a}_z \tag{5}$$

where superscript $(\cdot)'$ denotes complex conjugate transpose and $\overline{\overline{T}}_{uv}(\varphi,z)$ is a frequency and position-dependent $N\times N$ complex matrix defined by:

$$\overline{\overline{T}}_{uv}(\bar{r},f) \triangleq \begin{bmatrix} E_{u_1}(\bar{r}) \\ E_{u_2}(\bar{r}) \\ \vdots \\ E_{u_N}(\bar{r}) \end{bmatrix}\left[H_{v_1}^*(\bar{r})\ H_{v_2}^*(\bar{r})\ \ldots\ H_{v_N}^*(\bar{r})\right]; u,v\in\{\rho,\varphi,z\}. \tag{6}$$

The total time-average complex power $P_{C_{\text{Total}}}$ delivered to volume V enclosed by surface(s) S would be:

$$P_{C_{\text{Total}}}(\overline{A},f) = -\frac{1}{2}\oint_S \overline{A}\left[\left(\overline{\overline{T}}_{\varphi z}(\bar{r},f) - \overline{\overline{T}}_{z\varphi}(\bar{r},f)\right)\hat{a}_\rho + \left(\overline{\overline{T}}_{\rho\varphi}(\bar{r},f) - \overline{\overline{T}}_{\varphi\rho}(\bar{r},f)\right)\hat{a}_z\right]\overline{A}'\cdot\hat{a}_n ds. \tag{7}$$

Since $\overline{A}$ is independent of the integration variables, we can carry out the integrations for each element of $\overline{\overline{T}}_{uv}(\bar{r},f)$ by defining $\overline{\overline{Q}}$ matrices as:

$$\begin{cases}\left[\overline{\overline{Q}}_{\varphi z}(f)\right]_{m,n} = -\frac{1}{2}\oint_S\left(\left[\overline{\overline{T}}_{\varphi z}(\bar{r},f)\right]_{m,n} - \left[\overline{\overline{T}}_{z\varphi}(\bar{r},f)\right]_{m,n}\right)\hat{a}_\rho\cdot\hat{a}_n ds \\ \left[\overline{\overline{Q}}_{\rho\varphi}(f)\right]_{m,n} = -\frac{1}{2}\oint_S\left(\left[\overline{\overline{T}}_{\rho\varphi}(\bar{r},f)\right]_{m,n} - \left[\overline{\overline{T}}_{\varphi\rho}(\bar{r},f)\right]_{m,n}\right)\hat{a}_z\cdot\hat{a}_n ds\end{cases}; m,n=1\cdots N. \tag{8}$$

Now, by defining:

$$\left[\overline{\overline{Q}}_{\rho\varphi z}(f)\right]_{m,n} \overset{\text{def}}{=} \left[\overline{\overline{Q}}_{\varphi z}(f)\right]_{m,n} + \left[\overline{\overline{Q}}_{\rho\varphi}(f)\right]_{m,n}; m,n = 1\cdots N \tag{9}$$

Eq. (7) can be further simplified into a quadratic form suitable for optimization purposes as:

$$P_{C_{\text{Total}}}(\overline{A},f) = \overline{A}\,\overline{\overline{Q}}_{\rho\varphi z}(f)\overline{A}'\ (\text{W}). \tag{10}$$

Eq. (10) and its element-wise integrals in Eq. (8) are presented in cylindrical coordinates for an axisymmetric cryostat assembly but can be adapted to different forms and coordinate systems. The versatility of the surface integrals in Eq. (8) allows us to include areas that interact strongly with the gradient fields, notably near cryostat edges and side plates where magnetic fields generated by coils are not properly canceled. Simulations will show how these locations contribute to the overall ohmic power loss.

Due to the cylindrical symmetry for a z-gradient array coil, only H_z, H_ρ and E_φ exist, and they are independent of φ. This reduces the cylindrical closed-surface integrals in Eq. (8) down to $2\pi\rho$ times the "closed-path integrals" along the perimeter of the warm shield where ρ is the local radius of the closed path to be traversed. The fields and parameters are depicted in Figure 1. In Eq. (8), we choose S as the outer surface of the warm shield, and consequently, the closed path corresponds to the cross-section of the warm shield denoted by the ABCD blue double line in Figure 1. This choice proves useful because when the array coil operates in advanced mode,[11] it generates significant magnetic fields near the cryostat's end plates. The advanced mode of a gradient array coil provides a wide range of extra functionalities where the performance parameters such as the linearity, gradient strength, FOV position and diameter, and slew rate are programmable.[11] To the authors' knowledge, none of the published gradient array coil design and tuning approaches account for induced currents and associated power losses in the warm shield and both of the end plates.

Back to Eq. (8), both $\overline{\overline{T}}_{z\varphi}$ and $\overline{\overline{T}}_{\rho\varphi}$ are zero because of symmetry and only $\left[\overline{\overline{T}}_{\varphi z}\right]_{mn} = \left[E_\varphi H_z\right]_{mn}$ and $\left[\overline{\overline{T}}_{\varphi\rho}\right]_{mn} = \left[E_\varphi H_\rho\right]_{mn}$ exist and are used for integrations. By adjusting the limits and considering the direction of the unit vectors as $\hat{a}_\rho \cdot \hat{a}_n = \pm 1$ (AB or CD path) and $\hat{a}_z \cdot \hat{a}_n = \pm 1$ (BC or DA path), reduced surface integrals read:

$$\begin{cases} \left[\overline{\overline{Q}}_{\varphi z}(f)\right]_{m,n} = \pi\left[\int_A^B - \int_D^C\right]\rho\left[E_{\varphi_m}(\bar{r})\, H^*_{z_n}(\bar{r})\right]_{m,n} dz \\ \left[\overline{\overline{Q}}_{\rho\varphi}(f)\right]_{m,n} = \pi\left[\int_B^C - \int_A^D\right]\rho\left[E_{\varphi_m}(\bar{r})\, H^*_{\rho_n}(\bar{r})\right]_{m,n} d\rho \end{cases} ; m, n = 1 \cdots N. \tag{11}$$

After plugging the two $N \times N$ matrices into Eq. (9) and then Eq. (10), we arrive at the total time-average complex power $P_{C_{\text{Total}}}$ for a sinusoidal gradient waveform of frequency f, delivered into the warm shield. These one-time integral calculations are computed using the numerical data integration package of Maple®.[14] It is worth highlighting that the spatial resolution of the sampled E and H fields along the ABCDA path determines the time needed to populate the matrices.

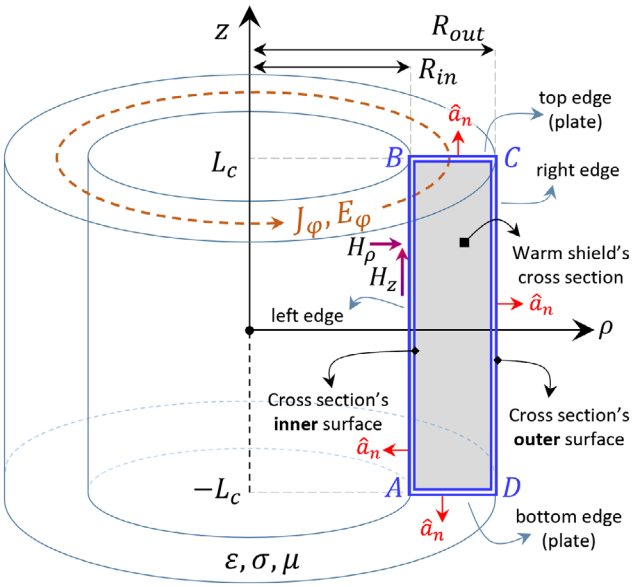

FIGURE 1 A typical cylindrical warm shield of length $2L_c$, radii R_{in} and R_{out} and body thickness d (the thick blue double line) and its cross-sectional view showing solely the inner and outer surfaces. None of the inner layers/components of the cryostat are considered here. The left, right, top, and bottom edges of the outer surface and the starting and end points of these edges (A–D) are shown and labeled. Both of the axial and radial net magnetic fields on the outer surface are shown as H_z, H_ρ. The current $J_\varphi = \sigma E_\varphi$ is also shown. The red $\hat{a}_n$ unit vectors are normal to the integration paths.

2.3 | Eddy power loss calculation for an arbitrary periodic excitation

Assume $g(t)$ as a (real-valued) periodic waveform of period T. Using the complex exponential representation of the waveform, one can write:

$$g(t) = \sum_{m=-\infty}^{\infty} c_m e^{j2\pi\frac{m}{T}t}, c_m = \frac{1}{T}\int_T g(t) e^{-j2\pi\frac{m}{T}t} dt. \tag{12}$$

The DC component c_0 has no contribution. Moreover $|c_{-m}|^2 = |c_m|^2$. Assuming $A_n(t) = A_n g(t)$ for $n = 1 \ldots N$, we can use Eq. (10) and deploy the superposition for the average power associated with each harmonic and calculate the grand total time-average eddy power loss as:

$$\begin{aligned} P_g^{\text{Loss}}(\overline{A}) &\cong \sum_{m=1}^{M} |2c_m|^2 \text{Re}\left\{P_{C_{\text{Total}}}\left(\frac{m}{T}\right)\right\} \\ &= \sum_{m=1}^{M} |2c_m|^2 \text{Re}\left\{\overline{A}\,\overline{\overline{Q}}_{\rho\varphi z}\left(\frac{m}{T}\right)\overline{A}'\right\} \end{aligned} \tag{13}$$

where M determines the number of harmonics such that the Fourier expansion in Eq. (12) resembles $g(t)$. The

level of resemblance can be determined by observing the decreasing trend of $|c_m|$. The frequency dependency of $\overline{\overline{Q}}_{uv}(f)$ in Eq. (11) means that a set of $\overline{\overline{Q}}_{uv}$ matrices at a relevant set of frequencies are needed to accurately carry out Eq. (13). Because the harmonic content of conventional MRI pulse sequences is limited, a handful number of these one-time $\overline{\overline{Q}}_{uv}$ calculations would suffice for all purposes.

2.4 | Eddy power loss calculation based on Fourier transform

Assume a periodic gradient pulse sequence, say $g(t)$, which is used to drive MRI gradient coils every T seconds. One can rewrite Eq. (13) as:

$$P^{\text{Loss}}_{g(t)}(\overline{A}) = \sum_{m=1}^{M} \left| \frac{2}{T} G\left(\frac{m}{T}\right) \right|^2 \text{Re}\left\{ \overline{A}\, \overline{\overline{Q}}_{\rho\varphi z}\left(\frac{m}{T}\right) \overline{A}' \right\} \tag{14}$$

where $G(f)$ is the Fourier transform of the pulse $g(t)$. It is important to note that both Eqs. (13) or (14) consist of two parts: (a) a truncated summation that depend on the shape of the feeding waveform and the number of harmonics used for approximation; (b) a quadratic expression in the form of $\overline{A}\overline{\overline{Q}}_{\rho\varphi z}(f)\overline{A}'$ that depends on the geometrical structure of the coil elements and their feeding currents as well as the harmonic frequency being excited. Such a separation between the waveform characteristics and coil shape helps us to focus mainly on the unknown feeding currents during the optimization process without involving the waveform itself.

2.5 | An analytic expression for the magnetic flux density of a z-gradient array coil

The wire pattern for a z-gradient coil consists of coaxial circular annular wires. The axial component of the magnetic flux density, B_Z, created by a filamentary circular wire loop of current I and radius a, at an arbitrary point of height h and radial distance ρ from its center is given by[15]:

$$B_z(a,\rho,h) = \frac{\mu_0 I}{2\pi\sqrt{(a+\rho)^2+h^2}} \left[K(k) + \frac{a^2-\rho^2-h^2}{(a-\rho)^2+h^2} E(k) \right],$$
$$k^2 = \frac{4a\rho}{(a+\rho)^2+h^2} \tag{15}$$

where K and E are the complete elliptic integrals of the first and second kinds. We assume the primary and shield array coils collectively consist of $N/2+N/2$ bundles of annular wire loops of current $A_i, i = 1 \ldots N$. The wire bundles (each with n_t turns) are uniformly spaced along the z-axis. The array's overall axial magnetic flux density B_z^{Arr} at an arbitrary point (ρ, z) inside and outside of the coil (except within the wires) can be written as:

$$B_z^{Arr}(\overline{A},\rho,z) = \sum_{i=1}^{Nn_t/2} \left\{ A_{\left\lceil \frac{i}{n_t} \right\rceil} B_z\left(R_p,\rho,z-w_{p,i}\right) + A_{\left\lceil \frac{N}{2}+\frac{i}{n_t} \right\rceil} B_z\left(R_s,\rho,z-w_{s,i}\right) \right\} \tag{16}$$

where '⌈ ⌉' denotes the ceil function and $w_{p,i}$ and $w_{s,i}$ are the primary and shield wire positions, respectively.[11] Given that the fields generated by eddy currents within the ROI are small in magnitude, the impressed longitudinal B_z field in this region primarily stems from the gradient coils, ensuring precise calculations of the B_z field becomes imperative. This precision is achieved through Eq. (16). It's worth noting that this equation is not employed for calculating the stray fields on or around the cryostat, as is commonly done in various articles. The rationale behind this distinction will be elaborated upon in subsequent discussions.

2.6 | Z-gradient coil structure and dimensions

Three cylindrical conducting structures comprise a typical cryostat assembly: a stainless steel warm shield at room temperature, an Aluminum cold shield at 50 K, and a stainless steel spool at 4.2 K.[16,17] We only include the warm shield and simulate the fields and then calculate the eddy power losses dissipated inside the warm shield. The cold shield and the spool and their dedicated ohmic power losses were not included to simplify the numerical computations by reducing the number of geometry discretizations. The 3D structure and its half-cross-sectional view of the cylindrical cryostat are shown in Figure 2A,B, respectively. All dimensions and essential details are included in the caption to shorten the text.

2.7 | Optimization procedure

When designing an active-shielded gradient array coil within a cryostat's presence, two main approaches could exist: (a) The first method involves computing the induced eddy currents on[12] (and more accurately inside) the cryostat's metallic body for all array elements. Secondary fields within the ROI are ignored during optimization. This is possible since the optimization process minimizes

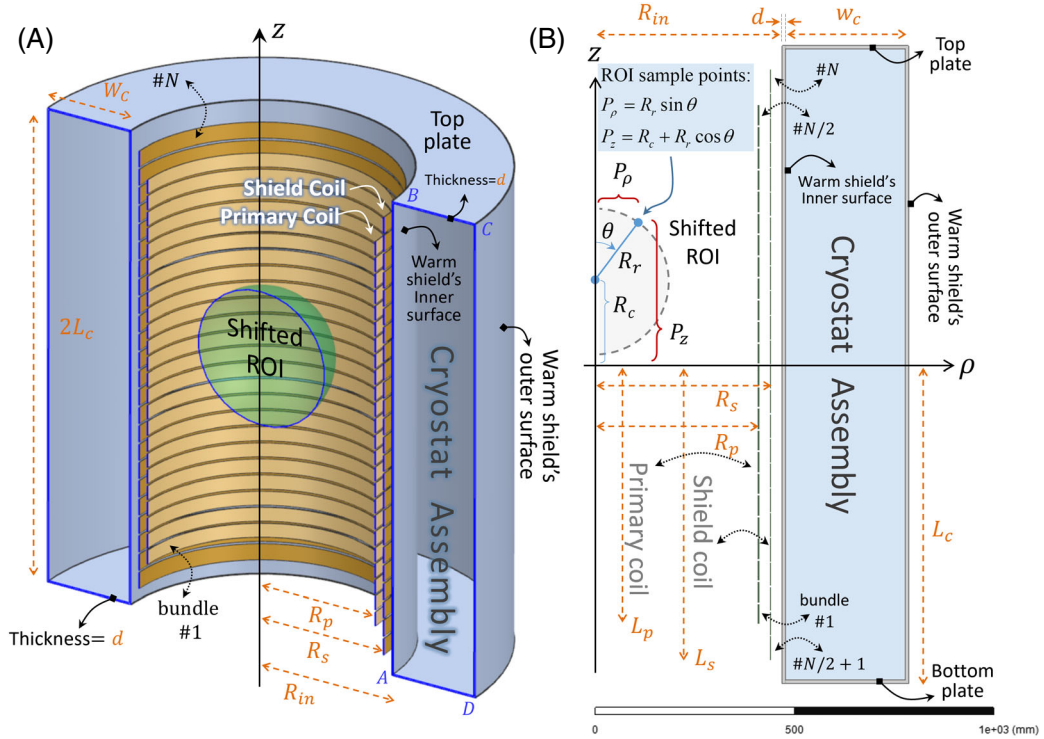

FIGURE 2 (A) The 3D structure of the proposed z-gradient array coils within a simplified cryostat subsystem (excluding the cold shield and the spool). It consists of the cylindrical warm shield of thickness $\boldsymbol{d = 5}$ mm, length $\boldsymbol{2L_c = 1.6}$ m, inner radius $\boldsymbol{R}_{\text{in}} = \boldsymbol{0.47}$ m and two welded end plates of width $\boldsymbol{W_c = 30}$ cm. (B) The half-cross-sectional view of (A) with some other details. The primary array bundles are labeled from #**1** to #$\boldsymbol{N/2}$, and the shield array is labeled from #$\boldsymbol{N/2+1}$ to #$\boldsymbol{N}$, with $\boldsymbol{N = 48}$. (B) The center and radius of the ROI are shown by $\boldsymbol{R_c}$ and $\boldsymbol{R_r}$. The radial distance and height of the field sampling point are shown by $\boldsymbol{P_\rho}$ and $\boldsymbol{P_z}$. (A) The ABCD corner point introduced in Figure 1 and the shifted ROI. The remaining coil parameters are: $\boldsymbol{2L_p = 1.3}$ m, $\boldsymbol{R_p = 41}$ cm, $\boldsymbol{2L_s = 1.48}$ m, and $\boldsymbol{R_s = 44}$ cm.

the eddy currents that create these secondary fields. (b) Alternatively, the second approach considers induced eddy currents within the cryostat and their secondary fields on and inside the ROI for each array element. Optimization is performed to achieve minimal eddy power loss within the cryostat and the best field profile within the ROI.

We opt for the first approach by enhancing the accuracy of calculating each array element's contribution to the total eddy losses. The overall eddy loss minimization directly reduces both the stray fields on the cryostat's surface and the secondary fields within the ROI. This choice requires less computation and ensures quicker responses, a critical factor for real-time magnetic profile adjustments. We are exploring the potential benefits of the second approach in our future work.

We deploy a series of distinct constraints for each target point on and inside the ROI to achieve precise control over the uniformity of the field gradient within the ROI, especially when it is shifted.[11] Additionally, in contrast to minimizing the stray fields on the outer surface of the warm shield, we attempt to minimize the time-average eddy power loss provided by Eq. (10) or either of Eqs. (13) or (14). This approach leads us to a quadratic minimization problem

$$\text{Given } f: \min_{\overline{A}} \left\{ \overline{A} \left[\alpha_{\text{eddy}} \text{Re}\left\{ \overline{\overline{Q}}_{\rho\varphi z}(f) \right\} + \alpha_{\text{store}} \text{Im}\left\{ \overline{\overline{Q}}_{\rho\varphi z}(f) \right\} + \alpha_{\text{copper}} \overline{\overline{R}}(f) \right] \overline{A}' \right\}, \tag{17}$$

subject to the following constraints:

$$\begin{cases} \frac{1}{B_{\text{ideal}}^{\max}} \left| B_z^{Arr}\left(\overline{A}, R_r \sin\theta_n, R_c + R_r \cos\theta_n\right) - G_z R_r \cos\theta_n \right| \le \varepsilon_{\text{ROI}}, & n = 1 \cdots N_{\text{ROI}} \\ \frac{1}{B_{\text{ideal}}^{\max}} \left| B_z^{Arr}\left(\overline{A}, 0, R_c + z_m\right) - G_z z_m \right| \le \varepsilon_{\text{ROI}} & m = -N_z \cdots N_z \\ |A_i| \le I^{max} & i = 1 \cdots N \end{cases} \tag{18}$$

where R_c and R_r (Figure 2B) are the center and radius of the ROI, G_Z is the desired gradient intensity, and $B_{\text{ideal}}^{\max} = G_z R_r$ is the expected maximum B_z^{Arr} field within the ROI. The first set in Eq (18) with $\theta_n = \pi(n/N_{\text{ROI}})$ enforces N_{ROI} distinct constraints on the right semicircle boundary of the ROI that guarantee the relative field deviations on the (shifted) ROI will not exceed ε_{ROI}. Note that for multiple or shifted ROIs,[18] the interior of the ROI should be included for the error assessment since maximum field deviation

does not always happen on the boundary. The second set of constraints insert an extra $2N_Z + 1$ points with $z_m = R_r(m/N_z)$ to control the linearity deviation along the z-axis. These constraints should be duplicated for as many ROIs[9] as needed and can be modified for non-spherical ROIs as well. The tuning coefficient, ε_{ROI}, controls the maximum field linearity error on and inside the (shifted) ROI, typically between 5% to 15%. α_{eddy} and α_{store} control the eddy loss and the stored magnetic energy within the structure. $\overline{\overline{R}}_{N\times N}(f)$ is a diagonal frequency-dependent resistance matrix (AC + DC) and α_{copper} controls ohmic power loss due to copper wires. For eddy loss minimization only, both $\alpha_{\text{store}} = \alpha_{\text{copper}} = 0$.

3 | RESULTS

For all matrix computations and dedicated optimizations, a CORE i7, 8th generation laptop with 12GB of memory and for EM simulations using Ansys Maxwell 2023.R1.1,[19] a Dell Precision 3650 workstation with an Intel® Xeon CPU (12 cores) and 128 GB of memory is used. The operating systems are Windows 10. In Eq. (18), we choose $I^{\max} = 300$ A, $N = 48$, $n_t = 22$, and $N_Z = 2$ that helps to search for a better gradient uniformity inside the (shifted) ROI within all possible solutions that could be a local minimum. To save memory and CPU time, we assume $W_c = 30$ cm rather than its typical width of $W_c = 1$ m.[17] The net EM fields generated by each array element are sampled by 0.2 mm resolution along the closed *ABCDA* path (see Figure 1) of length $2L_c + 2W_c + 4d = 382$ cm (> 19000 field points). The *IntegrateData* command of the Signal Processing package and the Nonlinear Programming Solver command (*NLPSolve)* of the Optimization package, both from Maple™ 2022 software, were deployed in this research. The optimizations in Eqs. (17) and (18) take no more than 5 s to converge and the 48×48 $\overline{\overline{Q}}$ matrices in Eq. (11) are populated in 65 s.

We consider the warm shield of the cryostat assembly to be composed of nonmagnetic Stainless Steel 304 material, serving as the initial passive shield. At a temperature of 300 K, its conductivity is approximately about $\sigma_{SS} = 1.388\times10^6$ S/m. As emphasized in Section 2.6, our assumption excludes any presence of additional lossy medium or a cold shield within the warm shield. This choice, driven by the twin objectives of simplicity and efficient computational execution for field simulations, leads to the fact that $\text{Re}\{\oint \overline{E}\times\overline{H}\cdot d\bar{s}\}$ is zero on the inner surface of the cryostat, obviating the need for field sampling in this region.

However, in scenarios where both the warm and cold shields are to be accounted for, as in practical cryostat designs, it becomes imperative to encompass the inner and outer surfaces of both shield layers in our considerations.

3.1 | Frequency selection for $\overline{\overline{Q}}_{uv}$

Induced eddy currents depend on the time derivative of applied magnetic fields. The greater the frequency, the stronger the coupling between the wires and the body of the cryostat, and thus the greater the eddy power loss. Figure 3 depicts the time-average eddy power loss $P^{\text{Loss}}_{\sin(\omega t)} = \frac{1}{2}\text{Re}\left\{\oint_S \overline{E}\times\overline{H}^*\cdot d\bar{s}\right\}$ under sinusoidal excitations for a given set of feeding currents, where S is the warm shield's surface. Additionally, $P^{\text{Loss}}_{\sin(\omega t)}/\sqrt{f}$ is also depicted by the dashed line to demonstrate its normalized frequency-dependent behavior. It begins at zero, has two break points, and finally remains almost constant after $f \geq 10$ kHz, for a wide range of excitations. Based on the high frequency content of the driving pulse sequence, one of the following approaches can be used:

1. If the effective high frequency components are concentrated around a frequency, say 1 kHz, choosing $\overline{\overline{Q}}_{\rho\varphi z}(f = 1\text{ kHz})$ would suffice to achieve a near optimal solution for the cost function Eq. (17).
2. If a wider range of high-frequency components exists, we may find a more optimal solution. Assume $F_{set} = \{f_1, f_2, \ldots, f_k\}$ as the set of k frequency components of $g(t)$ with the highest magnitudes and $c_{set} = \{c_1, c_2, \ldots, c_k\}$ as their corresponding magnitudes. Eq. (17) can be reformulated as:

$$\min_{\overline{A}} \text{Re}\left\{\overline{A}\left[\sum_{i=1}^{k}|c_i|^2\overline{\overline{Q}}_{\rho\varphi z}(f_i)\right]\overline{A}'\right\} \tag{19}$$

where α_{store} and α_{copper} are set to zero for simplicity. For both cases above, when the optimum $\overline{A}$ has been computed, either of Eqs. (13) or (14) can be used to calculate the total time-average eddy power loss $P^{\text{Loss}}_{g(t)}(\overline{A})$.

To accurately estimate eddy power loss for a non-sinusoidal waveform using Eqs. (13), (14), or (19), we compute and store sixteen 48×48 matrices for frequencies between 10 Hz and 30 kHz, namely $M_{set} = \{10, 30, 50, 80, 100, 300, 500, 800, 1\text{k}, 2\text{k}, 3\text{k}, 4\text{k}, 5\text{k}, 8\text{k}, 10\text{k}, 30\text{k}\}$. The last one is used to accurately extrapolate the loss curve for $f \geq 10$ kHz (see Figure 3). This is important for those pulse sequences with high-frequency components since they contribute the most in the power loss even with relatively small magnitudes of c_n.

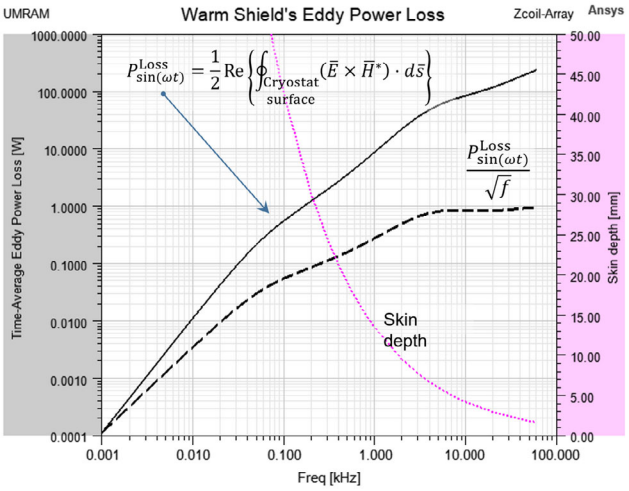

FIGURE 3 Time-average eddy power loss $\boldsymbol{P^{Loss}_{sin(\omega t)}}$ for a given set of sinusoidal feeding currents calculated on the warm shield's outer surface. The dashed line shows its normalized version $\boldsymbol{P^{Loss}_{sin(\omega t)}/\sqrt{f}}$ and demonstrates its frequency behavior that stars from zero, has two break points, and finally remains almost constant after $\boldsymbol{f > 10}$ kHz. The dotted purple line shows the skin depth as a function of excitation frequency.

The logarithmic magnitude plot of H_z, H_ρ, and E_φ (at $f = 1$ kHz) are plotted in Figure 4A–C. The horizontal axis represents the distance traversed by a closed *ABCDA* path (see Figure 1) of length 382 cm. The first (#1) and the last (#24) array elements of both primary and shield coils are labeled in the figure. These fields are simulated and stored for each array element at multiple frequencies when fed by a current of unity amplitude. A single frequency simulation that computes the EM fields for all array elements takes 77 min and consists of 117 k tetrahedra within the cryostat's body with maximum edge size of 1 mm. After computing the associated $\overline{\overline{Q}}$ matrices, we do not need them anymore.

3.2 | Stray field minimization method versus proposed method for z-gradient array coil tuning

We commence with two optimizations for the z-gradient array coil, both of which are subjected to similar constraints of <5.0% linearity deviation, 40.0 mT/m gradient strength, and 45 cm diameter of ROI. All array elements are excited by 1 kHz sinusoidal current sources of a maximum of 300A.

In the first optimization, we aim to nullify the stray fields on the cryostat while also reducing the copper loss within the wire coils. Driven by an optimization regarding the optimum number of field sampling points on the warm shield, the details of which are provided in the supporting Section (A) in Appendix S1, we consider 40 uniformly distributed distinct points $(z_i, i = 1 \ldots 40)$ along the left edge of the warm bore and minimize $\sum_{i=1}^{40}\left|B_z^{Arr}\left(\overline{A}, R_{in}, z_i\right)\right|^2 + \alpha_{copper}\sum_{i=1}^{48}A_i^2$ with $\alpha_{copper} = 5\times10^{-3}$. In this approach, the power losses incurred by induced eddy currents within the end plates are neither included nor minimized. However, in the second optimization that includes the entire cryostat (see Figure 2), the proposed method provided by Eq. (17) with $\alpha_{copper} = 5\times10^{-5}, \alpha_{store} = 0$, and $\alpha_{eddy} = 1$ is deployed. Figures 5 and 6 illustrate half-plots of both B_z and $|\boldsymbol{B}|$ fields for each optimization separately.

The first optimization converges in 16 s, resulting in a total time-average eddy power loss of 23.33 W, with contributions of 20.15 W from the left edge and 3.16 W from both end plates. The RMS value for all feeding currents is 190.2 A_{RMS}. Eq. (10) predicts 23.28 W, closely matching the simulation. In the second optimization, which converges in 3.9 s and covers the entire cryostat's warm shield, the values are 8.34 W (reported by Maxwell), 186 A_{RMS} (4.2 A less), and 8.32 W according to Eq. (10). The power loss contributions from the left edge and both end plates are 7.17 W and 1.16 W, respectively. Notably, this new approach significantly outperforms the stray field method, reducing power loss by more than 2.8 times while achieving even lower RMS current.

3.3 | Power loss calculation for an arbitrary waveform

After selecting the dominant high frequency and running the optimization, the excitation vector $\overline{A}$ is ready for eddy loss calculation for an arbitrary waveform, $g(t)$. We proceed by calculating 15 distinct $\overline{A}\,\overline{\overline{Q}}_{\rho\varphi z}(f)\overline{A}'$ values using M_{set} matrices and then perform interpolation for all harmonic contents of $g(t)$ in this range. For harmonic frequencies above 10 kHz a logarithmic extrapolation is utilized. Assuming f_0 as the fundamental harmonic of $g(t)$, the total time-average eddy power loss will be:

$$P^{Loss}_{g(t)} = \sum_{m=1}^{M}|2c_m|^2 p_m; \tag{20}$$

$$p_m \overset{def}{=} \begin{cases} \text{interpolate}\left[\mathrm{Re}\left\{\overline{A}\,\overline{\overline{Q}}_{\rho\varphi z}(f)\overline{A}'\right\}\right]_{f=mf_0} & f \le 10\text{ kHz} \\ \text{extrapolate}\left[\mathrm{Re}\left\{\overline{A}\,\overline{\overline{Q}}_{\rho\varphi z}(f)\overline{A}'\right\}\right]_{f=mf_0} & f > 10\text{ kHz} \end{cases}.$$

We investigate two scenarios. As the first scenario, we consider the second optimization provided in Section 3.2

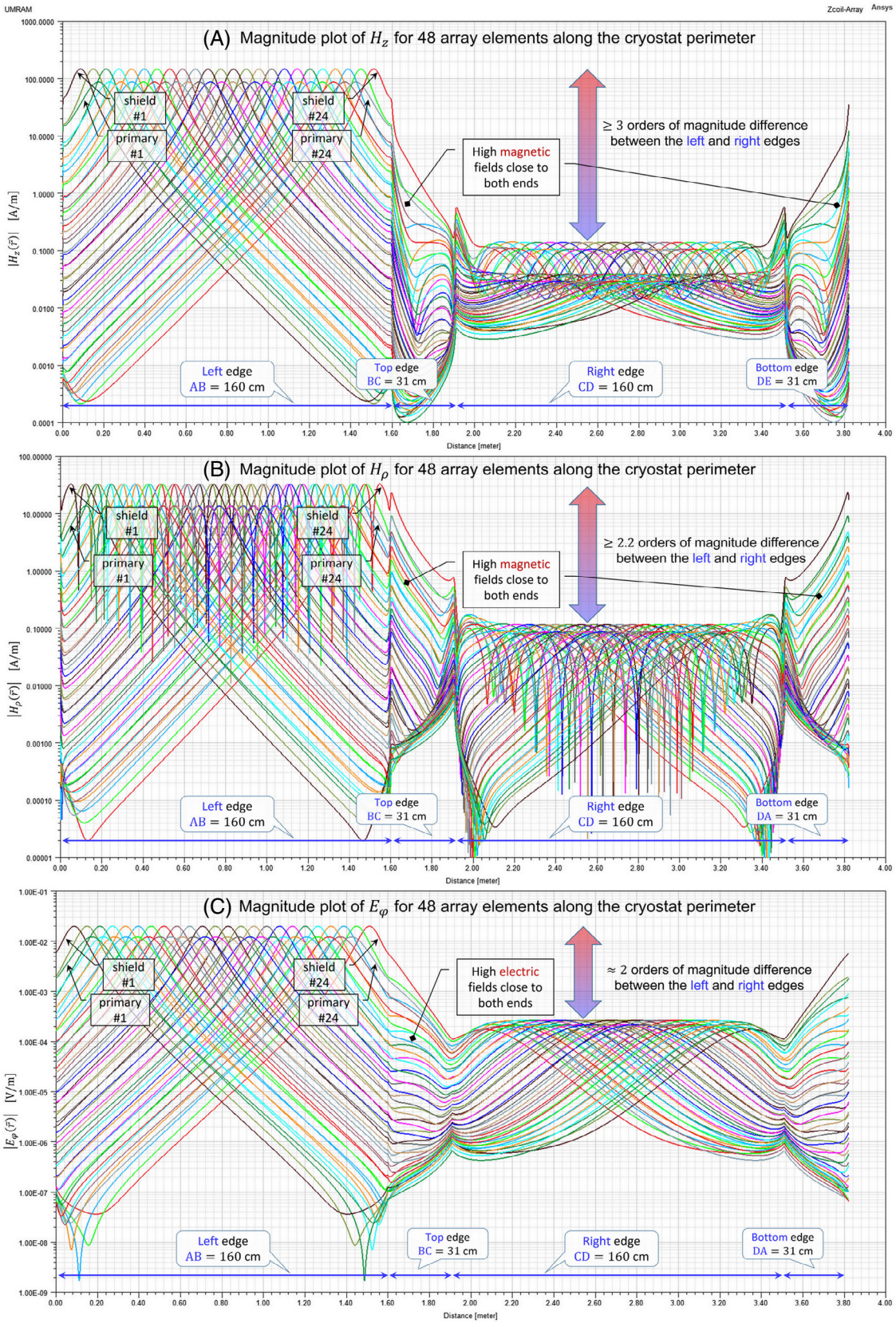

FIGURE 4 The logarithmic magnitude plot of $\boldsymbol{H_z}$,$\boldsymbol{H_\rho}$ and $\boldsymbol{E_\varphi}$ versus distance by traversing ABCDA path in Figure 1. The path includes 160 cm left edge, 31 cm top edge, 160 cm right edge, and 31 cm bottom edge. Although the left and right edge field values differ by at least two orders of magnitude, the fields at close proximity of both ends and along the plates cannot be ignored. The first (#1) and the last (#24) array elements of both primary and shield coils are labeled in the picture.

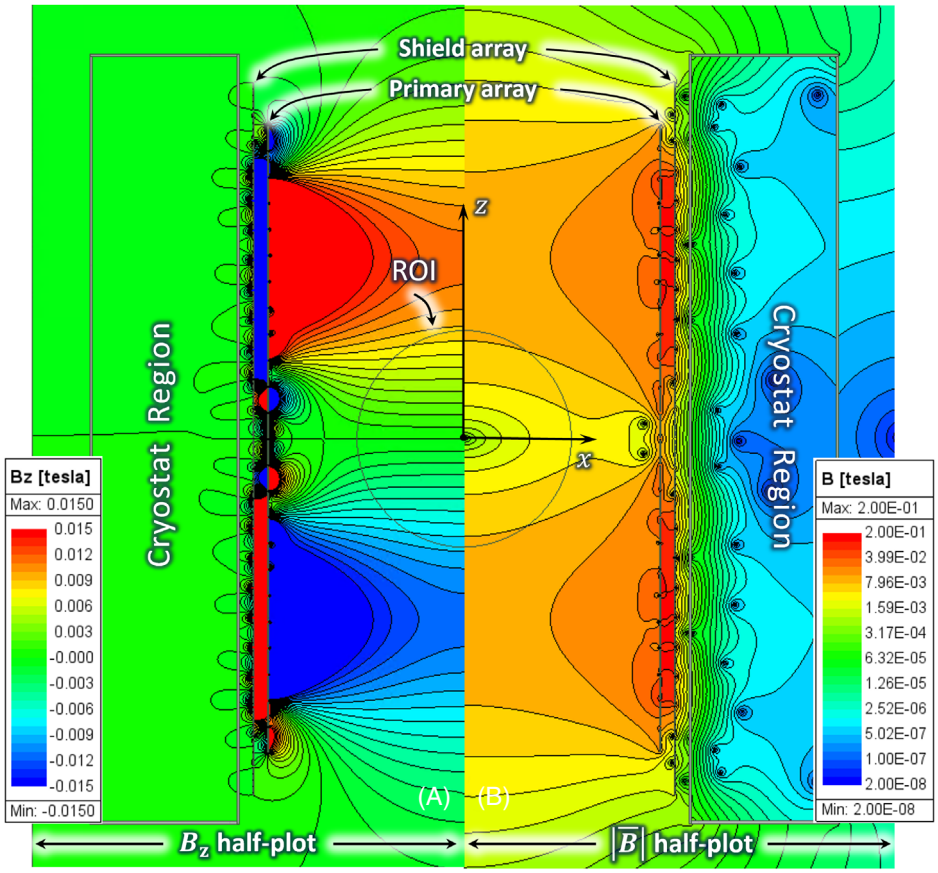

FIGURE 5 Half plots of (A) $\boldsymbol{B_z}$ field map and (B) $|\overline{\boldsymbol{B}}|$ field map for the first design by nullifying the stray fields on 40 distinct points on the left edge of the warm shield that takes 16 s to converge. The array coils, the ROI, and the thin body of the warm shield as well as the cryostat region are shown. The diameter of the ROI is 45 cm. The linearity error and gradient strength within the ROI are 5.26% and 40.1 mT/m, respectively. The RMS value of all feeding currents is 190.2 A. The average eddy power loss (reported by Maxwell) is 23.33 W, where the contributions of the left edge, right edge, and both end plates are 20.15 W, 0.020 W, and 3.16 W, respectively. For the complete cryostat assembly, the proposed formulation in Eq. (10) reads 23.28 W.

which was only based on $\overline{\overline{Q}}_{\rho\varphi z}$ at $f = 1$ kHz. Figure 7 shows 10 cycles of eddy power loss (and its running average) within the cryostat. Details of the feeding waveform $g(t)$ are given in the caption. Eq. (20) predicts 32.83 W (with $M = 20$ harmonics) which agrees well with the 31.80 W running average shown in the transient simulation with about 3% error. In the second scenario, the relevant $\overline{\overline{Q}}_{\rho\varphi z}$ matrices are weighted by dominant harmonics of the driving waveform to acquire a multi-frequency $\overline{\overline{Q}}_{\rho\varphi z}$ matrix. For the same bipolar trapezoid waveform with 2, 4, 6, 8, and 10 kHz as the dominant harmonics, $|c_m|^2$ reads 0.78, 0.16, 0.043, 0.024, and 0.001, respectively. By running the minimization in Eq. (19), a new set of currents with 185A_{RMS} can be found. Eq. (20) predicts 30.86 W of average power loss (not shown in the figure), which is 6% less than the first scenario.

3.4 | Power loss calculation for a pulse sequence

We assume $g(t)$ as a general bipolar trapezoidal waveform of amplitudes A_1, A_2 and break-points a, b, c, d, e as shown in Figure 8A and $w(t)$ as its repeated version by N times followed by a blank signal that extends up to $t = L$ and then repeats indefinitely (see Figure 8B). Using Eq. (12) and assuming $0 < a \le b < c \le d < e \le L/N$, c_n is given by:

$$c_n = \frac{L}{4n^2\pi^2} \cdot \frac{PD(0,Ne)}{PD(0,e)} \cdot \Big[-\frac{A_1}{a} PD(0,a) + \frac{A_1 - A_2}{c-b} PD(b,c) + \frac{A_2}{e-d} PD(d,e) \Big], \tag{21}$$

where $PD(t_1, t_2)$ is the phase difference function defined by:

$$PD(t_1,t_2) \overset{\text{def}}{=} e^{-j2n\pi(t_1/L)} - e^{-j2n\pi(t_2/L)}. \tag{22}$$

Note that A_1/a, $A_2/(e-d)$ and $(A_1 - A_2)/(c-b)$ represent the slew rates of $g(t)$ during the rise and fall times, respectively. Similar analytic expressions can be found for other commonly used pulse sequences. Using Eqs. (21) and (22), one can find the dominant harmonics of a given pulse sequence and use one of two optimization cost functions in Eqs. (17) or (19) to solve for unknown currents $\overline{A}$. Once the currents are found, Eq. (20) can be used for power loss estimation.

As the last optimization example, we consider a symmetric pulse sequence consisting of $N = 4$ bipolar (± 1) trapezoidal pulses of 400 μs rise and fall times (between -1 and 1) and 200 μs plateau times, collectively repeated every $L = 10$ ms ($a = 200\mu$s, $b = 400\mu$s, $c = 800\mu$s, $d = 1$ ms, and $e = 1.2$ ms). Figure 8C shows the power

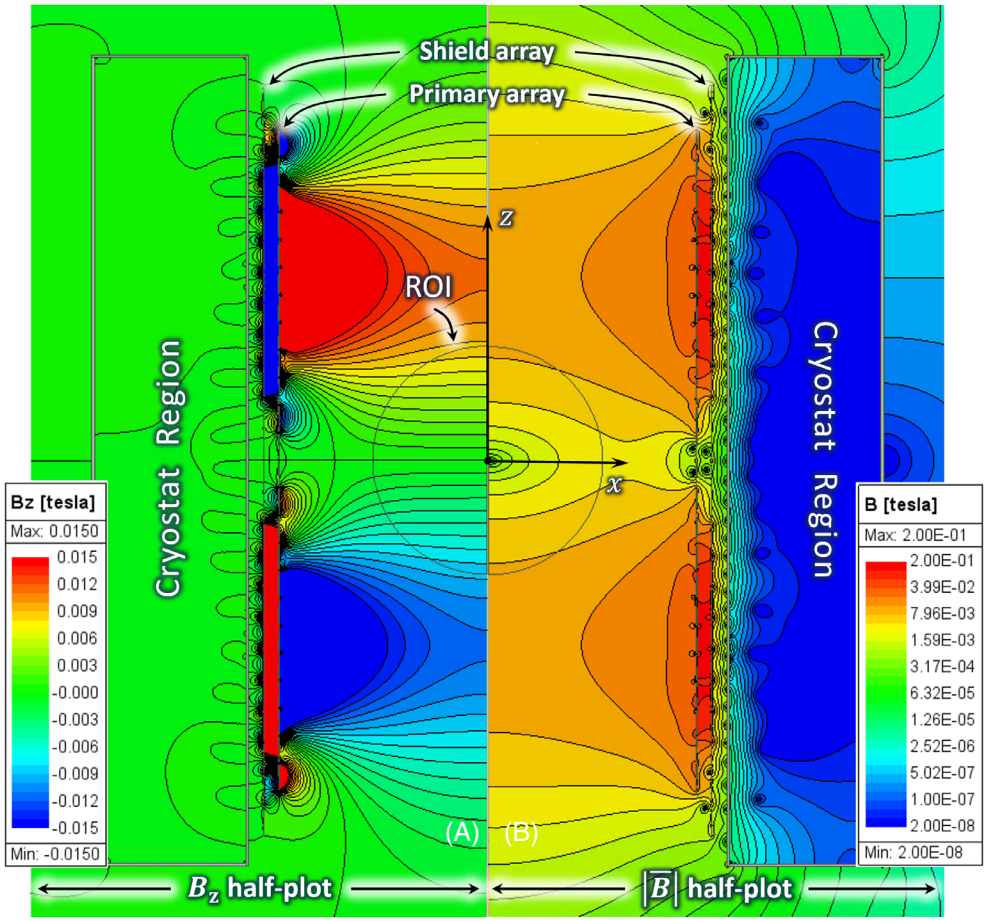

FIGURE 6 Half plots of (A) $\boldsymbol{B_z}$ field map and (B) $|\overline{\boldsymbol{B}}|$ field map for the second design based on the proposed cost function. It takes care of all four edges (the whole surface) and takes 3.9 s to converge. The diameter of the ROI is 45 cm. The linearity error and gradient strength within the ROI are 5.18% and 40.2 mT/m, respectively. The RMS value of all feeding currents is 186 A (4.2 A less than Figure 5). Maxwell reports 8.34 W for the time-average eddy power loss in the cryostat. The power loss contributions from the left edge, right edge, and both end plates are 7.17 W, 0.01 W, and 1.16 W, respectively. The proposed formulation reads 8.32 W, which is 2.8 times less than the first design.

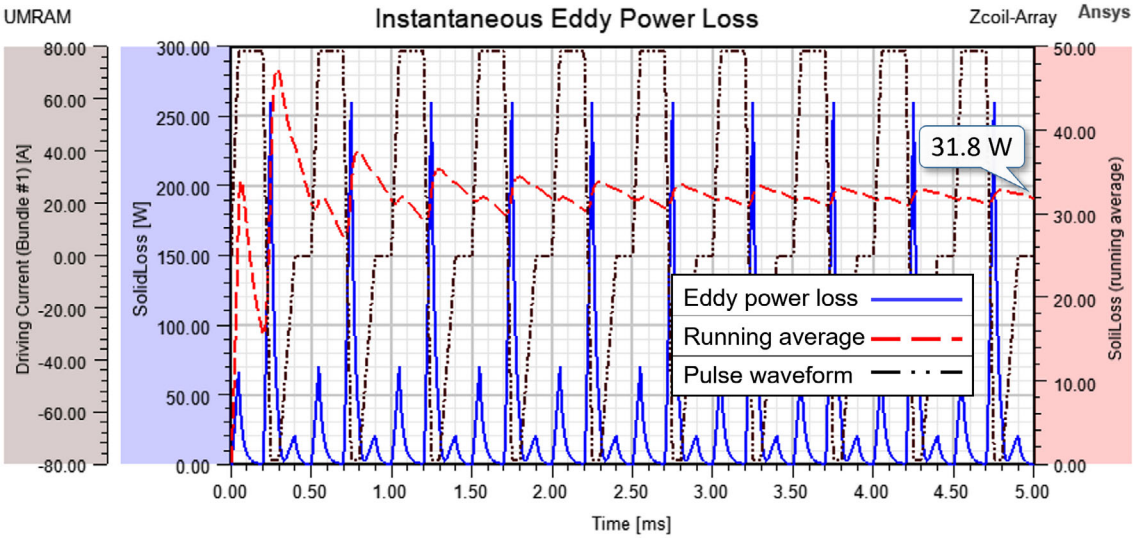

FIGURE 7 The feeding waveform used to drive the array elements is a 500us periodic bipolar trapezoidal waveform of 50 & 100 μs rise/fall time(s) and 50 & 150 μs plateau time(s) shown by black (dot-dot-dash line). A transient simulation based on the proposed optimization that illustrates 10 cycles of the instantaneous eddy power loss in (blue) and its running average within the cryostat (dashed red). Eq. (13) predicts 32.83 W (with $M = 20$ harmonics) which agrees well with the 31.80 W running average shown in the transient simulation with about 3% error. The RMS value of all feeding currents is 187.6 A.

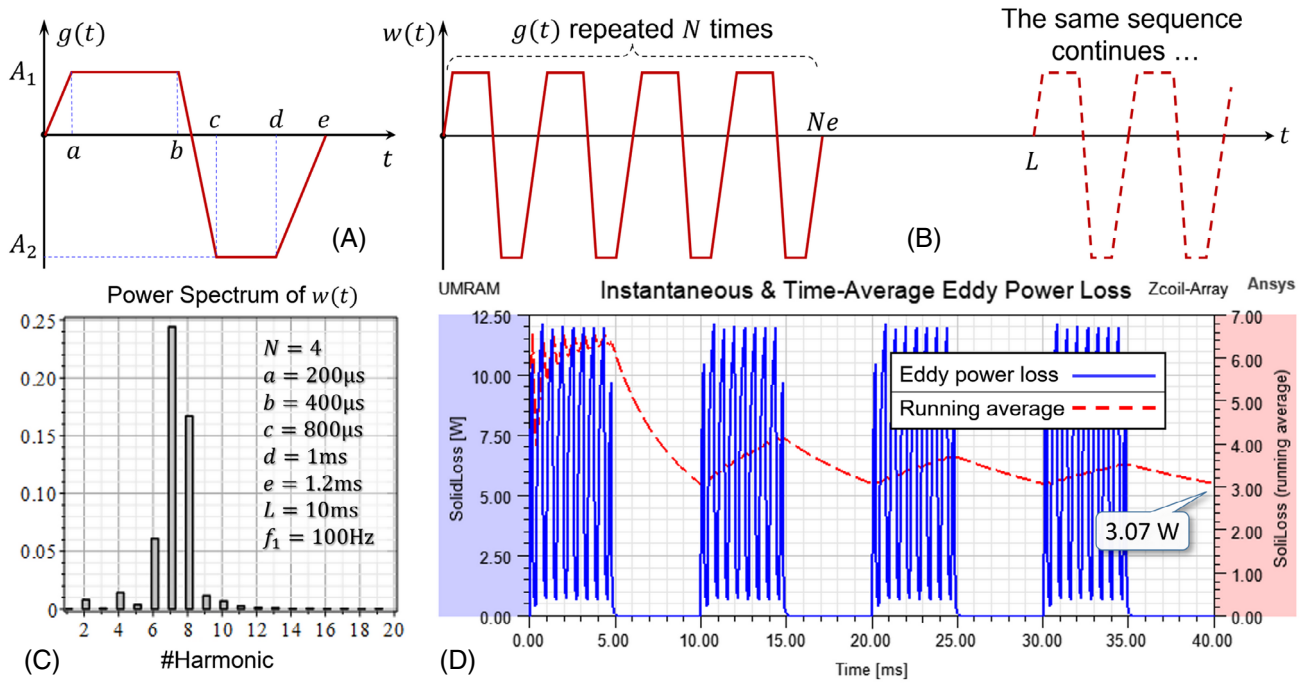

FIGURE 8 (A) $\boldsymbol{g(t)}$ is a bipolar trapezoidal pulse of amplitudes $\boldsymbol{A_1, A_2}$ and breakpoints $\boldsymbol{a, b, c, d, e}$. (B) $\boldsymbol{w(t)}$ is an $\boldsymbol{N}$ times repeated version of $\boldsymbol{g(t)}$, followed by a blank signal that extends up to $\boldsymbol{t = L}$ and then repeats indefinitely. (C) Power spectrum of $\boldsymbol{w(t)}$ for $\boldsymbol{N = 4}$, $\boldsymbol{a = 200\ \mu s}$, $\boldsymbol{b = 400\ \mu s}$, $\boldsymbol{c = 800\ \mu s}$, $\boldsymbol{d = 1\ ms}$, $\boldsymbol{e = 1.2\ ms}$, and $\boldsymbol{L = 10\ ms}$ with dominant harmonics around 700 Hz. (D) four full cycles of the transient simulation showing the instantaneous eddy power loss (and its running average) for $\boldsymbol{t = 10,\ 20,\ 30,}$ and **40** ms. The approach based on Eq. (20) reports 3.24 W power loss and 186 A_{RMS}. Ansys simulation reads 3.077 W, which is about 5% lower and agrees well with the proposed method.

spectrum of the pulse sequence. It is seen that 7th and 8th harmonics (700 Hz and 800 Hz) are the dominant ones. We use single frequency (800 Hz) optimization based on Eq. (17) since it is already in M_{set}. Additionally, $\alpha_{copper} = 5 \times 10^{-5}$ is used to reduce the RMS value. Our approach based on Eq. (20) reports 3.24 W power loss and 186 A_{RMS}. Figure 8D illustrates four full cycles of the transient simulation showing the instantaneous eddy power loss (and its running average) for $t = 10, 20, 30$, and 40 ms. Ansys simulation reads 3.077 W, which is about 5% lower and agrees well with the proposed method.

4 | DISCUSSION

The cross-sectional view in Figure 1 is a simplified version of a typical cylindrical cryostat assembly that does not include other internal components. This means that Eq. (10) solely predicts the total complex power delivered to what is inside the surface S (including both electrical and mechanical losses). If other components are inserted in the cryostat assembly, their precise shape, dimension, and materials must be included in the simulations to obtain accurate results. Additionally, the Poynting-based power (or energy) calculations must be performed twice, once on the warm shield's outer surface and once on its inner surface, with the difference determining the power loss specific to the warm shield's metallic body. The cryostat's cold shield and other metallic layers can be treated similarly.

A more in-depth examination of the physical behavior of the EM fields on and inside the cryostat's metallic body (see the supporting Section (B) in Appendix S1) reveals why the proposed approach is more effective than the stray field minimization method. Since the cryostat's body is a thin lossy medium rather than a perfect conductor, the induced eddy currents within the warm shield are affected not only by the surface magnitude of the stray fields but also by the rate of change of the magnetic field in both the radial and longitudinal directions.[13] Minimizing the tangential component of the $\overline{H}$ (or $\overline{B}$) field on the surface only addresses the magnitude and ignores how these fields penetrate the surface, vanish inside the body, and form the eddy current. The Poynting theorem accounts for all losses within a given volume without directly involving the field behavior inside the volume.

Simulations show that for different sets of sinusoidal excitation currents, the curve in Figure 3 shifts up or down, reflecting the amount of power loss, but the break-points remain almost stationary with only a slight shift to the left or right. To clarify the frequency response of $P^{\text{Loss}}_{\sin(\omega t)}$, the skin depth plot

has been added to the figure. Our observations are as follows: (a) When the skin depth approaches the thickness of the warm shield's thin metallic body, around $f \geq 6$ kHz, the induced eddy currents start vanishing when they penetrate the body. At higher enough frequencies, the EM fields are almost absorbed within the body, and hereafter, the power loss is proportional to $\sqrt{f}$. An approximate mathematical proof is provided in the supporting Section (C) in Appendix S1. (b) The frequency response of induced eddy currents for individual array elements differs amongst array elements. This is caused by the various radii and position of the array elements, and consequently, the level of coupling between these elements and the cryostat. (c) There are six orders of magnitude difference in the cryostat power loss (from 10^{-4} to 100 W) versus four orders of magnitude change in the excitation frequency (from 1 Hz to 10 kHz). Such a big variation means that for an excitation pulse containing a wide variety of harmonic components, it is better to deploy Eq. (19) rather than Eq. (17) to gain optimum results.

Similarly, the results illustrated in Figure 4 reveal that: (a) The magnitudes of the fields at the left edge (AB), which is closer to the gradient coils, are at least two orders of magnitude (three orders for the H_z field) greater than those at the right edge (CD). Therefore, the calculations for the right edge may be safely ignored. (b) Because of the warm shield's proximity, shield array elements have stronger fields and contribute more to eddy currents than primary array elements. (c) The field variations around both end plates (BC and DA) are much sharper and deeper for H_z rather than those for both H_ρ and E_φ that necessitate finer meshes at the corners. (d) For each array element, the magnitude ratio between the axial and radial components $\left(H_z/H_\rho\right)$ is at least 35 everywhere at the left edge; however, they may reach the same level at the top and bottom edges. The higher the frequency, the greater this ratio becomes, implying that at high enough frequencies, the normal component of the magnetic field vanishes, and only the tangential components need to be considered (as explained in the supporting Section (C) in Appendix S1).

5 | CONCLUSIONS

We propose a novel method based on a computational electromagnetic approach to estimate and regulate the time-average eddy power loss within the cryostat assembly, which improves the tuning of a gradient array coil of any shape given a pulse sequence. Compared to the stray field minimization method for a cylindrical cryostat assembly, the proposed approach results in more than 280% less power loss. The advantages are fourfold: (a) it addresses power losses within the cryostat body rather than just the outer cylindrical surface of the warm shield; (b) it accelerates array tuning and provides an accurate estimation for power losses or stored magnetic energies; (c) its accuracy is comparable to numerical results reported by commercial software; and (d) it is extendable to other array coils of any shape or even conventional coils.

ACKNOWLEDGMENTS

This work is fully funded by the Scientific and Technological Research Council of Turkey (TÜBİTAK) under the Grant No. 121E128.

ORCID

Manouchehr Takrimi https://orcid.org/0000-0001-5515-2472
Ergin Atalar https://orcid.org/0000-0002-6874-6103

REFERENCES

1. Hidalgo-Tobon SS. Theory of gradient coil design methods for magnetic resonance imaging. *Concepts Magn Reson*. 2010;36A:223-242. doi:10.1002/cmr.a.20163
2. Turner R. A target field approach to optimal coil design. *J Phys D Appl Phys*. 1986;19:L147-L151. doi:10.1088/0022-3727/19/8/001
3. Zhang R, Xu J, Fu Y, et al. An optimized target-field method for MRI transverse biplanar gradient coil design. *Meas Sci Technol*. 2011;22:125505. doi:10.1088/0957-0233/22/12/125505
4. Sanchez Lopez H, Poole M, Crozier S. Eddy current simulation in thick cylinders of finite length induced by coils of arbitrary geometry. *J Magn Reson*. 2010;207:251-261. doi:10.1016/j.jmr.2010.09.002
5. Juchem C, Nixon TW, McIntyre S, Rothman DL, de Graaf RA. Magnetic field modeling with a set of individual localized coils. *J Magn Reson*. 2010;204:281-289. doi:10.1016/j.jmr.2010.03.008
6. Jia F, Littin S, Layton KJ, Kroboth S, Yu H, Zaitsev M. Design of a shielded coil element of a matrix gradient coil. *J Magn Reson Imaging*. 2017 Aug;281:217-228. doi:10.1016/j.jmr.2017.06.006
7. Smith E, Freschi F, Repetto M, Crozier S. The coil array method for creating a dynamic imaging volume. *Magn Reson Med*. 2017 Aug;78:784-793. doi:10.1002/mrm.26404
8. Babaloo R, Takrimi M, Atalar E. Increasing Peripheral Nerve Stimulation Thresholds Using Gradient Array Coils. *Proceedings of the 30th Annual Meeting of ISMRM*, London, UK; 2022 Abstract #0580.
9. Ertan K, Taraghinia S, Sadeghi A, Atalar E. A z-gradient array for simultaneous multi-slice excitation with a single-band RF pulse. *Magn Reson Med*. 2018 Jul;80:400-412. doi:10.1002/mrm.27031
10. Ertan K, Taraghinia S, Sarıtas EU, Atalar E. Local optimization of diffusion encoding gradients using a z-gradient array for echo time reduction in DWI. *Proceedings of the 26th Annual Meeting of ISMRM*, Paris; 2018 Abstract #3194.
11. Takrimi M, Atalar E. A z – gradient array coil with a dedicated active-shielded array coil for MRI. *Magn Reson Med*. 2022;88:2718-2731. doi:10.1002/mrm.29390
12. Kassahun HB, Alsharafi SS, Badawi AM, El-Sharkawy AMM. Multi-Channel, actively shielded, power efficient MRI Z-gradient cylindrical coil design using target-field

method. *IEEE Access*. 2022;10:103840-103851. doi: 10.1109/access.2022.3210194
13. Jackson JD. *Classical Electrodynamics*. 3rd ed. Wiley; 1999:810.
14. Maple 2022. *Maplesoft, a Division of Waterloo Maple Inc*. Accessed October 05, 2023. Available at: https://www.maplesoft.com
15. Paul CR. *Inductance: Loop and Partial*. Wiley; 2010:379.
16. Breneman B. In: Harris RK, Wasylishen RL, eds. *History, Physics, and Design of Superconducting Magnets for MRI*. eMagRes; 2019:137-156.
17. Niu C, Wang L, Wang Y, et al. Numerical analysis of Eddy current induced by z-gradient coil in a superconducting MRI magnet. *IEEE Trans Appl Supercond*. 2020;30:1-6. doi:10.1109/tasc.2020.2969398
18. Takrimi M and Atalar E. MRI hybrid gradient coil equipped with a programmable Z-array and conventional X- and Y- elements. In Proceedings of the 29th Annual Meeting of the ISMRM, Virtual Conference; 2021 Abstract #3099.
19. https://www.ansys.com/products/electronics. Accessed Sep 10, 2023.
20. Sanchez Lopez H, Freschi F, Trakic A, et al. Multilayer integral method for simulation of eddy currents in thin volumes of arbitrary geometry produced by MRI gradient coils. *Magn Reson Med*. 2014;71:1912-1922.
21. Alsharafi SS, Badawi AM, El-Sharkawy AE-MM. Eddy currents analysis methods for an MRI longitudinal gradient coil. *Magn Reson Med Sci*. 2023;90:2158-2174. doi:10.1002/mrm.2977

SUPPORTING INFORMATION

Additional supporting information may be found in the online version of the article at the publisher's website.

Appendix S1. Supporting Information.

How to cite this article: Takrimi M, Atalar E. Minimization of eddy power loss in the cryostat for a z-gradient array coil driven by an arbitrary pulse sequence: An electromagnetic approach. *Magn Reson Med*. 2023;1-14. doi: 10.1002/mrm.29921